Supplement of Hydrol. Earth Syst. Sci., 25, 4681–4699, 2021
https://doi.org/10.5194/hess-25-4681-2021-supplement

Hydrology and Earth System Sciences
Open Access

Supplement of

How does water yield respond to mountain pine beetle infestation in a semiarid forest?

Jianning Ren et al.

Correspondence to: Jennifer C. Adam (jcadam@wsu.edu)

Supplement

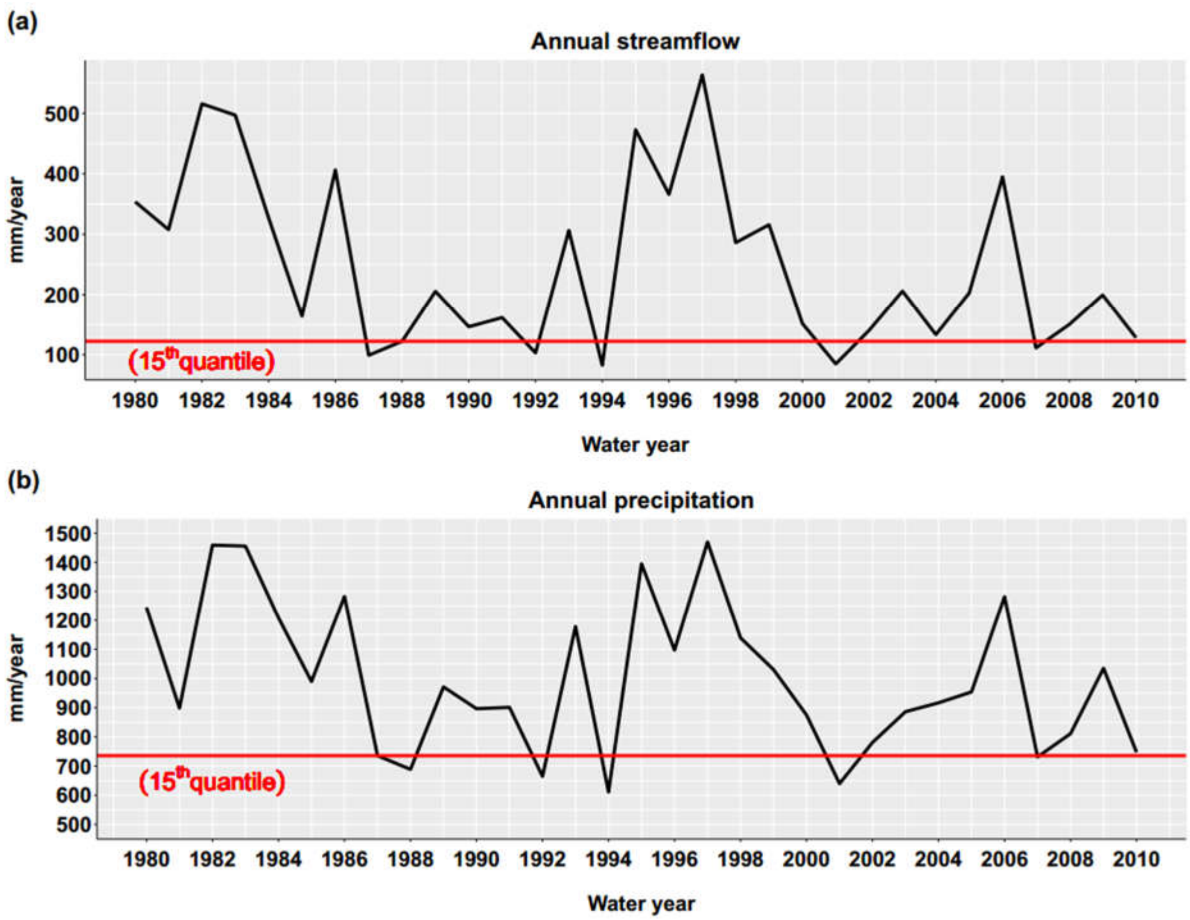

Figure S1. The annual streamflow and precipitation for Trail Creek. The red line is the 15th quantile of flow duration curves. Years with streamflow below the red line is water deficit years (dry years).

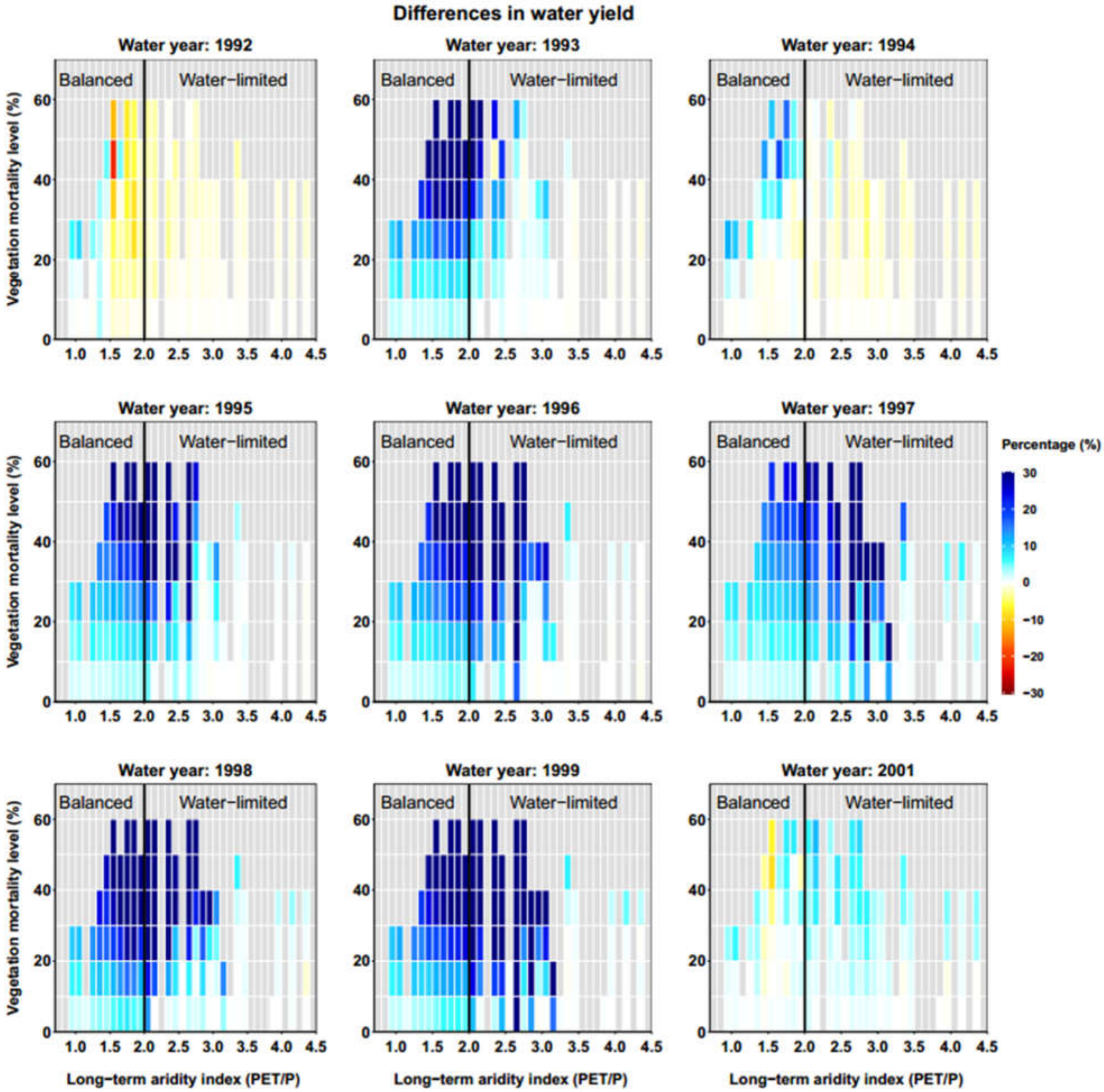

Figure S2. Relationship among long-term aridity, vegetation mortality level and Differences in water yield for 2-12 years after beetle outbreak (except for 2000).

1 Description of soil hydrologic model for RHESSys

The basic soil hydrologic model for RHESSys is described in detail in Tague and Band (2004) and updates described in other papers. We will provide a brief synopsis below.

In RHESSys, vertical and lateral soil moisture fluxes are modeled at the patch scale (i.e., the smallest grid cell), and the connectivity between patches is organized at the subbasin scale (meaning there is a closed water budget for each subbasin in the larger watershed). RHESSys uses a 4-layer model for vertical soil moisture processes, including a surface detention store, a root accessible store, an unsaturated store below rooting depths, and a saturated store. The vertical processes also include snowpack and litter moisture stores. All vegetation layers and a litter layer can also store water through interception.

In RHESSys, rain throughfall from multiple canopy layers and a litter layer provide potential infiltration. If precipitation is snow, snow throughfall updates a snowpack store. A simplified energy budget model is used to compute snowmelt. Surface detention storage receives water through net throughfall from canopy layers and snowmelt at a daily time step. Then water infiltrates into the soil following the Phillip (1957) infiltration equation. Within the daily time step, the ponded water that is not infiltrated is added to detention storage, and any water that is above detention storage capacity generates overland flow.

Infiltration updates one of three possible stores: a saturated store in cases where water table is at the surface, a rooting zone storage, or an unsaturated store for unvegetated patches. A portion of infiltrated water is assumed to bypass the rooting zone and unsaturated store via macropores. This bypass flow directly updates a hillslope scale deeper groundwater store. Vertical drainage occurs from the unsaturated store or rooting zone store based on hydraulic conductivity.

Capillary rise can move water from saturated zone to rooting zone or unsaturated store. The potential capillary rise is based on the equation from Eagleson (1978). Capillary rise is used to fill unsaturated zone to field capacity. To consider the sub-daily plant responses, 50% of capillary rise is allocated to the unsaturated zone at the beginning of the day. The rest of potential capillary rise is used to supply plant transpiration demands at the end of that day. Evaporation is computed from surface detention, surface soil and interception stores and transpiration from rooting zone or, in some cases saturated stores, using a Penman-Monteith approach.

The saturated store is modelled as a saturation deficit. Lateral fluxes occur via subsurface flow between patches or via a deeper hillslope scale groundwater flow model. Subsurface flow between patches follows topography and varies with saturation deficit and transmissivity. Transmissivity is computed as follows.

A vertical hydraulic conductivity profile is used to compute both vertical and lateral soil moisture fluxes. The saturated hydraulic conductivity, $K_{sat}(z)$ is calculated as

$$K_{sat}(z) = K_{sat_0} \, exp^{(\frac{-z}{m})} \quad (1)$$

K_{sat_0}: hydraulic conductivity at the surface

m: the decay rate of conductivity with depth

z: depth

Due to uncertainty in measured conductivity profiles and preferential flow, we need to calibrate m and K_{sat_0} against observed streamflow values. Soil porosity - $\emptyset(z)$ also changes with depth using the following equation:

$$\emptyset(z) = \emptyset_0 \, exp^{\frac{-z}{p}} \quad (2)$$

$\emptyset_0$: surface porosity which is a soil specific parameter

p: decay of porosity with depth

At a given profile section, the saturated soil moisture storage is computed by integrating porosity over the corresponding depth.

The drainage from the unsaturated zone to the saturated zone is controlled by two factors: field capacity of the unsaturated zone, and the vertical unsaturated hydraulic conductivity at the boundary separating the two layers. The relative saturation at field capacity is integrated over the porosity profile (from the surface to water table depth) to calculate the unsaturated zone soil moisture depth at field capacity. For this paper, the Clapp and Hornberger (1978) pedo-transfer model was used to determine the relative saturation at field capacity. Deeper groundwater flow is modelled as a simple linear aquifer.

2 Model parameterization

2.1 Model initialization

We initialized soil carbon and nitrogen pools using a traditional spin up to steady state approach (no changes in decadal average soil carbon and nitrogen stocks). Then we applied a target driven method (Hanan et al. 2018) to initialize vegetation carbon and nitrogen stores. This method allows vegetation to grow to target values based on remote sensing data, which enables us to initialize mixed-age, disturbance-prone landscapes, while still providing mechanistic stability and accounting for local resource limitation (e.g. local climate, nutrients, and groundwater availability) (Hanan et al. 2018). For Trail Creek, we set our targets using LAI, which we calculated using Landsat-5 TM reflectance data with a resolution of 30 meters. We chose the clearest available growing-season scene closest to the streamflow calibration start date of 10

November 2010; the selected scene (Path 40, Row 30) was acquired on 02 August 2010. We calculated the Normalized Difference Vegetation Index (NDVI) from TM images using Eq. (3).

$$NDVI = \frac{\rho_{NIR} - \rho_R}{\rho_{NIR} + \rho_R} \tag{3}$$

In this equation, ρ_{NIR} is the reflectance in the near-infrared part of electromagnetic spectrum and ρ_R is the reflectance in the red part (Hanan et al. 2018). The NDVI is used to estimate LAI by a generalized NDVI-LAI model developed by Baret et al. (1989) as following Eq. (4).

$$LAI = -\frac{1}{k} \times \ln\left(\frac{NDVI_{\infty} - NDVI}{NDVI_{\infty} - NDVI_{back}}\right) \tag{4}$$

Here, *k* represents the extinction of solar radiation through a canopy. $NDVI_{\infty}$ is the maximum $NDVI$ of the region, and $NDVI_{back}$ is the background NDVI (i.e., pixels without vegetation) for each vegetation region. We get *k* value from Smith et al. (1991) for mixed pine and from White et al. (2000) for other vegetation types (Hanan et al. 2018). The other parameters are calculated for each vegetation in each image (Table S1)

Table S1. Normalized difference vegetation index – leaf area index (NDVI – LAI) model parameters for different vegetation types in Trail Creek.
k is the extinction of solar radiation through a canopy, $NDVI_{\infty}$ is maximum NDVI observed in different vegetation types, and $NDVI_{back}$ is the background NDVI (not considering vegetation) for different vegetation types.

Vegetation	k	$NDVI_{\infty}$	$NDVI_{back}$
Pine	0.42	0.66	0.01
Deciduous	0.54	0.67	0.17
Grass	0.48	0.73	0.01
Shrub	0.55	0.71	0.06

2.2 Model calibration and evaluation

We calibrated the coupled model against observed streamflow, which is from USGS gauge no. 13137500. Six subsurface soil parameters were calibrated: saturated hydraulic conductivity (K_{sat}), the decay of K_{sat} with depth (*m*), pore size index (*b*), air-entry pressure (φ_{ae}), bypass flow to deeper groundwater storage (gw_1), and deep groundwater drainage rates to stream (gw_2). To account for the spatial variability of precipitation within each gridMET 4-km grid cell, we also calibrated a parameter that is used for interpolating grid-scale precipitation along elevation gradients. We selected the best parameter set by comparing observed and modeled streamflow using a multi-objective function, which includes daily Nash-Sutcliffe efficiency metric (*NSE*; Nash and Sutcliffe 1970), Monthly *NSE*, percent error (*PerErr*) in annual flow estimates, and Pearson's Correlation Coefficient (*r* values larger than 0.5 are considered to be a good fit). *NSE* is used to compare the model fit to peak flows and it ranges from $-\infty$ to 1, where 1 means perfect fit and below zero means that the mean of the observation is more accurate than the simulated value. *PerErr* is used to compare differences between modeled and observed streamflow volumes.

In addition to evaluating calibrations on streamflow, we also compared basin-scale simulated ET with the Moderate Resolution Imaging Spectroradiometer (MODIS) based global data product (Zhao et al. 2006; Mu et al. 2007; Zhang et al. 2009; Mu et al. 2011), and compared simulated snowpack with Snow Telemetry data (SNOTEL, NRCS). These additional assessments are used to determine whether good streamflow fits are for the right reasons (i.e., the important processes are captured by the model). Seven years (2011 – 2017) of streamflow data, 15 years (1991-2015) of SNOTEL data (Lost-Wood Divide station), and 13 years (2003 – 2015) of MODIS ET data are used for this calibration and evaluation process (without special notification, we are using "water year"). As to the streamflow dataset, the first five water years are used for calibration and the last two years are used for evaluation.

3 Model parameterization results

3.1 Model initialization result

By using the target driving method, RHESSys successfully captured LAI heterogeneity across the landscape during initialization process. As shown in Figure S3 a and b, the initialized LAI matches well with remote sensing product, though some patches may slightly overshot because of the way RHESSys allocates carbon to LAI seasonally; while some other patches, mostly at the top of mountains and being covered by rock or snow, are initialized with near-zero LAI but remote sensing products shows some higher values. The median of simulated LAI is 3.6% higher than median of remotes sensing product. Overall, the simulated LAI for model initialization is in a reasonable range.

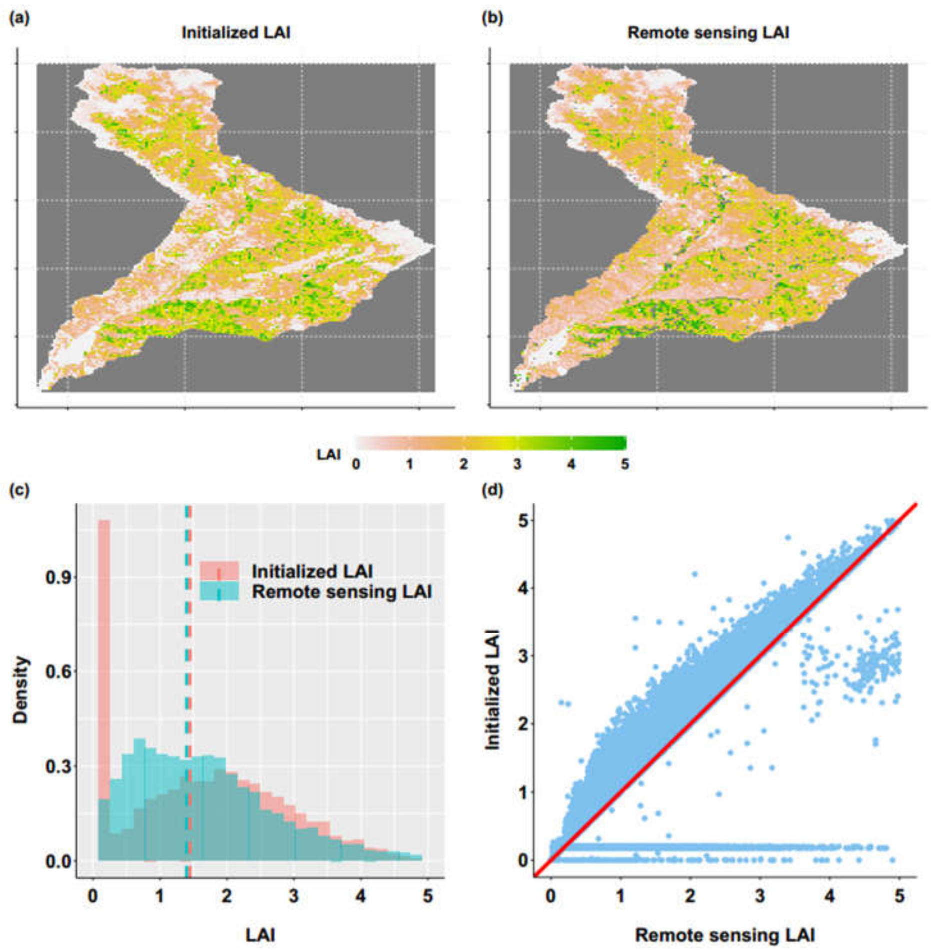

Figure S3. Vegetation initialization results. We calculated LAI from a remote sensing image and use it as the target to initialize vegetation carbon and nitrogen for trail creek. (a) is LAI initialized from RHESSys model using the target-driven method (Hanan et al. 2018). (b) is the target LAI calculated from remote sensing data (LANDSAT 5). (c) is a comparison of the density distributions of LAI for the remote sensing and model initialized, dashed line is the mean of two LAI distributions. (d) is the scatter plot of remote sensing LAI and initialized LAI

3.2 Model calibration and evaluation results

In general, the model performs satisfactorily in simulating streamflow, with slightly better performance during the calibration period than during the evaluation period (Fig. S4 and Table S2). The model can capture the seasonality of streamflow, i.e., matching peak, recession, and low flow periods. However, in some water years (e.g., 2015-2016), the timing of simulated peak flows show large bias since the model generates earlier streamflow (Fig. S4 and Table S2). This is likely because RHESSys uses air temperatures to partition precipitation into rain and snow and when it is near freezing, the partition errors might be large (Lundquist et al. 2008). This limitation can cause poor simulation of streamflow and ET in those years, but the influence and bias for modeling long-term ecohydrological fluxes are likely small (Bart et al. 2016). To further test the RHESSys performance on snow accumulation, we compare the simulated snow water equivalent (SWE) with SNOTEL data for the water years 1990-2015. The daily NSE is 0.93 and PerError is -14%, which is in acceptable range due to this being a patch-level comparison and not a basin-scale aggregation (which generally leads to higher model performance estimation). We also compare simulated ET with MODIS ET for water years 2002-2017 and they show similarities in annual mean and standard deviations, i.e. 725±62 mm/year and 702± mm/year from the simulation and MODIS, respectively. In summary, model performance on streamflow is roughly consistent for calibration and evaluation periods; the model also does a reasonably good job in estimating long-term average of SWE and ET.

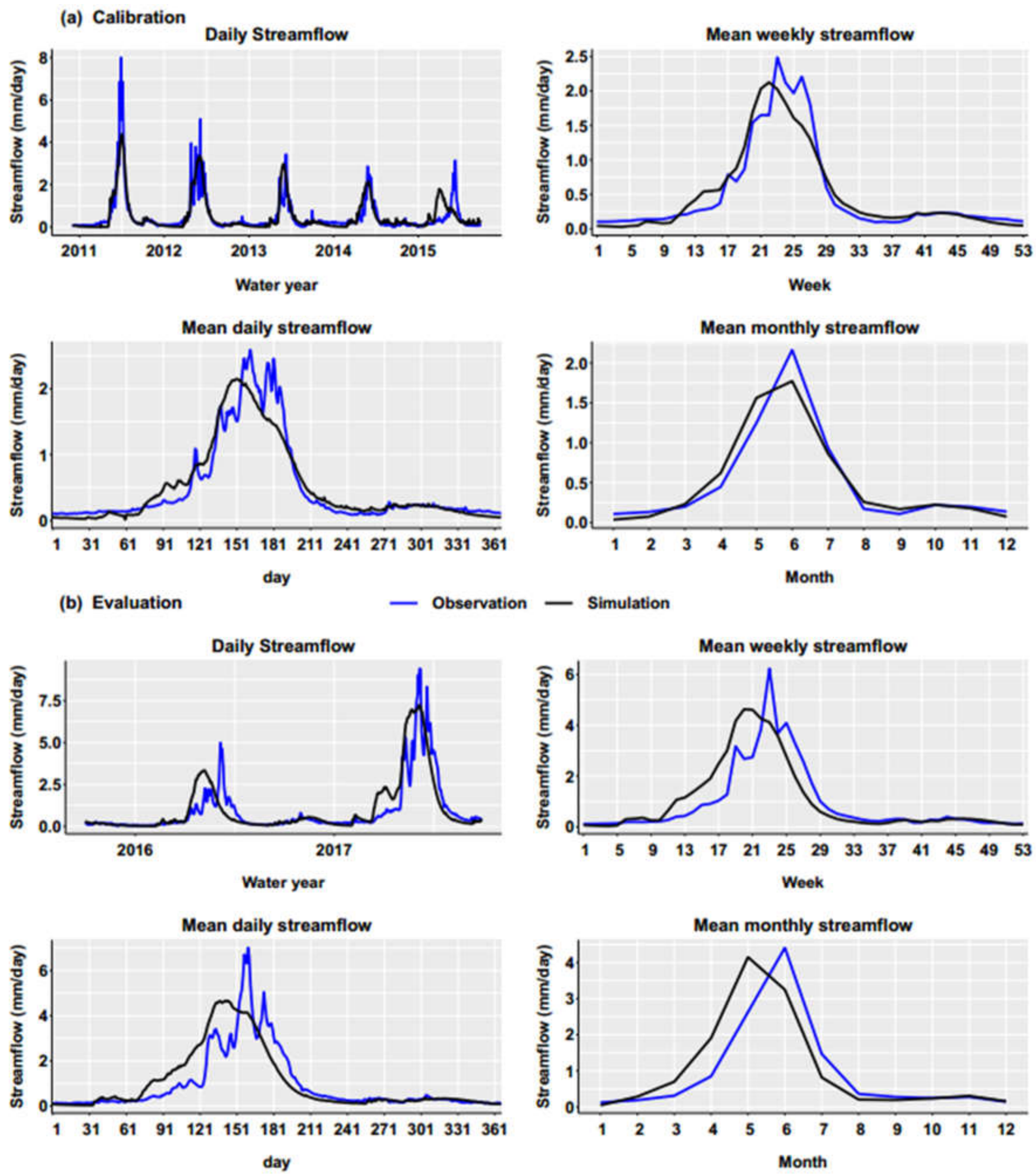

Figure S4. Model calibration and evaluation in streamflow. (a) is result during calibration period (i.e., 2011 to 2015), and (b) is results during evaluation period (i.e., 2016-2017).

Table S2. *Calibration and evaluation results for Trail Creek. NSE is Nash Sutcliff Efficiency and PerErr is total percent error, r is Pearson's correlation Coefficient. NSE is used for comparison of model fit of peak flows, PerErr is used to compare the differences in streamflow volumes, and r is used as a criterion to select better fit, which we consider r larger than 0.5 is a good fit.*

	Daily NSE	Monthly NSE	Percent error (%)	Pearson's correlation coefficient (r)
Calibration period (2011-2015)	0.76	0.94	2.66	0.76
Evaluation period (2016-2017)	0.71	0.73	8.62	0.74

4 Spatial result

4.1 Live LAI and Total LAI

Figure S5 shows the relationship among long-term aridity index (x-axis), vegetation mortality level (y-axis, for each sub-basin vegetation mortality is calculated as evergreen mortality multiplied by evergreen coverage of that sub-basin) and changes in LAI. Live LAI decreased after beetle outbreak and decreases were larger with increasing vegetation mortality (Fig. S5 a&b). Similarly, Total LAI decreased after beetle outbreak (and with increasing mortality) but the magnitude of LAI decreases were smaller compare to Live LAI (Fig. S5 c&d). In the water-limited region, Total LAI slightly increased after outbreak. The positive change in Total LAI occurred because, during the years of 1994 and 1995, some portion of dead foliage was still falling to the ground, while the living vegetation and understory canopy of some sub-basins grew faster than before due to less competition for resources, such as water, nitrogen, and solar radiation, so that Total LAI was higher than without beetle outbreak. From 1994 to 1995, some portion of dead foliage continued to fall to the ground, while the residual vegetation and understory continued to grow at higher rates (again, due to less competition for resources, such as water, nitrogen, and radiation). If increases in growth outstripped the rate of litterfall for dead foliage, there would be smaller Total LAI differences in 1994 as compared to 1995, and vice versa. The Live LAI response after outbreak affects plant transpiration, and Total LAI affects evaporation.

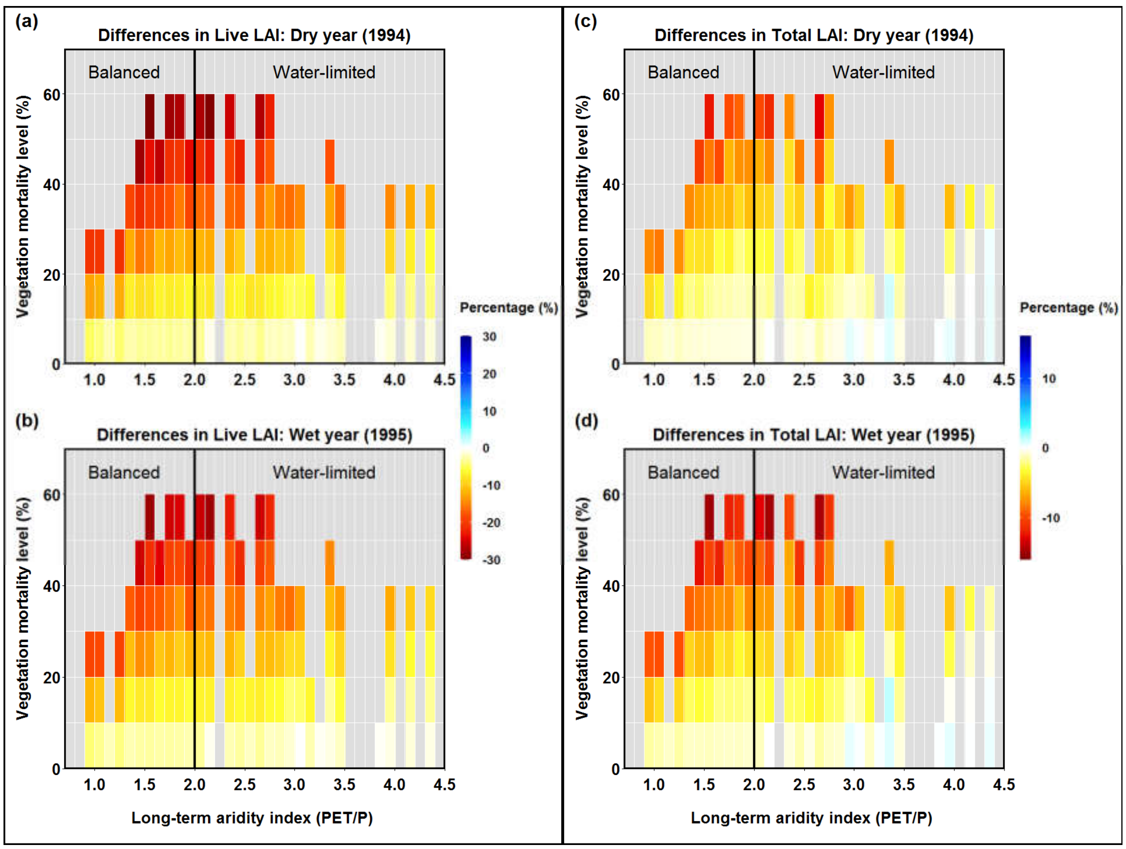

Figure S5. Relationship among long-term aridity, vegetation mortality, and differences in Leaf Area Index. Differences are calculated as the normalized differences (%) of LAI between each evergreen mortality scenario and the control run for no beetle outbreak. Vegetation mortality for each sub-basin is calculated as the percentage of evergreen patches multiplied by the mortality level of evergreen caused by beetles. Long-term aridity is defined as temporally averaged (38 years) potential evapotranspiration relative to precipitation. (a) and (c) are for a dry year (1994, 5 years after beetle outbreak),(b) and (d) are for a wet year (1995, 6 years after beetle outbreak). (a) and (b) is Live LAI while (c) and (d) is Total LAI (i.e., LAI including dead foliage and live leaf on the canopy).

4.2 Spatial result: year-to-year soil storage change

The effects of beetle outbreak on year-to-year soil storage change show a conversed spatial pattern during the dry year comparing with that during the wet year (Fig. S6). During a dry year, the balanced area charges water in soil storage, while the water-limited area loses water from soil storage. This spatial pattern matches well with effects of ET, which indicates that ET might be the primary driver of the change in soil moisture during dry years (Fig. 9a & Fig. S6a). During the wet year, the pattern conversed from that during the dry year: the balanced area shows decreases in soil moisture, while the water-limited area shows increases (Fig. S6b). Obviously, this pattern is different from that of ET (Fig. 9b & Fig. S6b). The balanced area, under high precipitation condition (i.e., wet year), experiences less ET causing the soil saturated much earlier than control scenario therefore, more precipitation will generate runoff. On the other hand, the water-limited area, under high precipitation conditions, experiences less ET meaning more precipitation will be stayed in the soil.

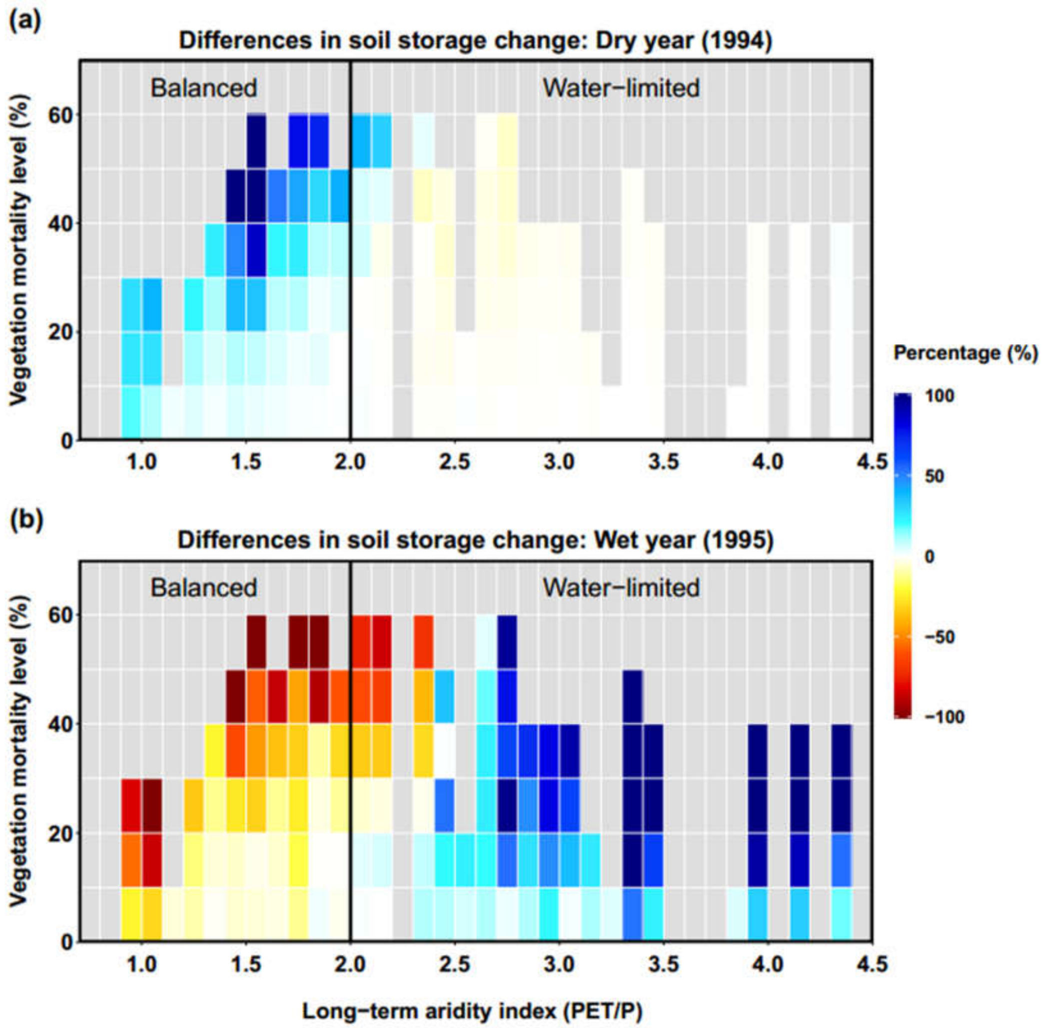

Figure S6.Relationship among long-term aridity, vegetation mortality level and Differences in year-to-year soil storage change for a dry year (1994, a) and wet year (1995, b).

5. Basin-scale snow sublimation responses after beetle outbreak

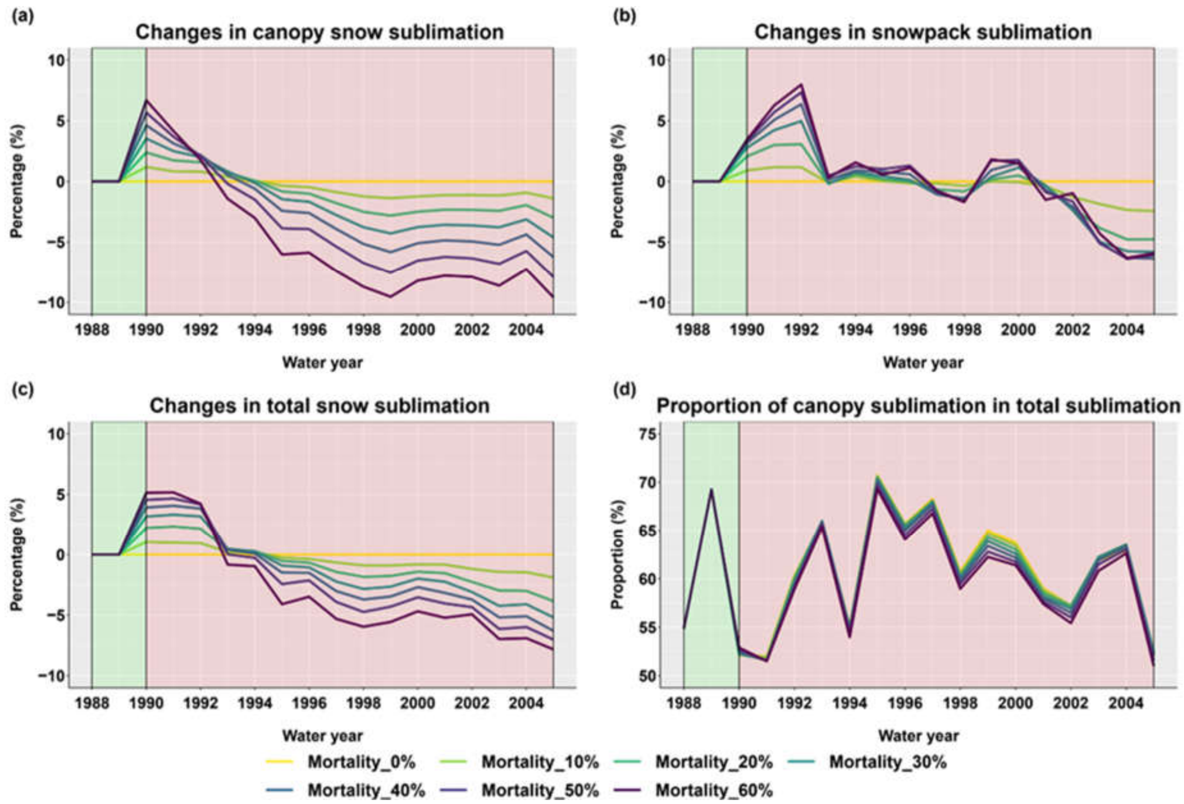

Figure S7. Basin-scale snow sublimation responses after beetle outbreak for different evergreen mortality levels. (a) changes (mortality scenario minus control scenario) in terms of percentage in canopy snow sublimation. (b) changes in snowpack sublimation. (c) Changes in total snow sublimation (canopy snow + ground snowpack). (d) the proportion of canopy snow sublimation in total sublimation.

References:

Baret, F., A. Olioso, J. L. Luciani, J. F. Hanocq, and J. C. Monterrot. 1989. “Estimation à partir de mesures de réflectance spectrale du rayonnement photosynthétiquement actif absorbé par une culture de blé.” *Agronomie* 9 (9): 885–95. https://doi.org/10.1051/agro:19890906.

Bart, Ryan R., Christina L. Tague, and Max A. Moritz. 2016. “Effect of Tree-to-Shrub Type Conversion in Lower Montane Forests of the Sierra Nevada (USA) on Streamflow.” Edited by Julia A. Jones. *PLOS ONE* 11 (8): e0161805. https://doi.org/10.1371/journal.pone.0161805.

Clapp, R., and G. Hornberger. 1978. “Empirical Equations for Some Soil Hydraulic Properties.” *Water Resources Research* 14: 601–4.

Eagleson, Peter S. 1978. “Climate, Soil, and Vegetation: 3. A Simplified Model of Soil Moisture Movement in the Liquid Phase.” *Water Resources Research* 14 (5): 722–30. https://doi.org/10.1029/WR014i005p00722.

Hanan, Erin J., Christina Tague, Janet Choate, Mingliang Liu, Crystal Kolden, and Jennifer Adam. 2018. “Accounting for Disturbance History in Models: Using Remote Sensing to Constrain Carbon and Nitrogen Pool Spin-Up.” *Ecological Applications: A Publication of the Ecological Society of America* 28 (5): 1197–1214. https://doi.org/10.1002/eap.1718.

Lundquist, Jessica D., Paul J. Neiman, Brooks Martner, Allen B. White, Daniel J. Gottas, and F. Martin Ralph. 2008. “Rain versus Snow in the Sierra Nevada, California: Comparing Doppler Profiling Radar and Surface Observations of Melting Level.” *Journal of Hydrometeorology* 9 (2): 194–211. https://doi.org/10.1175/2007JHM853.1.

Mu, Qiaozhen, Faith Ann Heinsch, Maosheng Zhao, and Steven W. Running. 2007. “Development of a Global Evapotranspiration Algorithm Based on MODIS and Global Meteorology Data.” *Remote Sensing of Environment* 111 (4): 519–36. https://doi.org/10.1016/j.rse.2007.04.015.

Mu, Qiaozhen, Maosheng Zhao, and Steven W. Running. 2011. “Improvements to a MODIS Global Terrestrial Evapotranspiration Algorithm.” *Remote Sensing of Environment* 115 (8): 1781–1800. https://doi.org/10.1016/j.rse.2011.02.019.

Nash, J. E., and J. V. Sutcliffe. 1970. “River Flow Forecasting through Conceptual Models Part I — A Discussion of Principles.” *Journal of Hydrology* 10 (3): 282–90. https://doi.org/10.1016/0022-1694(70)90255-6.

NRCS. n.d. “SNOTEL.” https://www.wcc.nrcs.usda.gov/about/mon_automate.html.

Phillip, J. 1957. “The Theory of Infiltration: 4. Sorptivity and Algebraic Infiltration Equation.” *Soil Sci* 84: 257–64.

Smith, Frederick W., D. Arthur Sampson, and James N. Long. 1991. “Comparison of Leaf Area Index Estimates from Tree Allometrics and Measured Light Interception.” *Forest Science* 37 (6): 1682–88. https://doi.org/10.1093/forestscience/37.6.1682.

Tague, C. L., and L. E. Band. 2004. “RHESSys: Regional Hydro-Ecologic Simulation System—An Object-Oriented Approach to Spatially Distributed Modeling of Carbon, Water, and Nutrient Cycling.” *Earth Interactions* 8 (19): 1–42. https://doi.org/10.1175/1087-3562(2004)8<1:RRHSSO>2.0.CO;2.

White, Michael A., Peter E. Thornton, Steven W. Running, and Ramakrishna R. Nemani. 2000. “Parameterization and Sensitivity Analysis of the BIOME–BGC Terrestrial Ecosystem

Model: Net Primary Production Controls." *Earth Interactions* 4 (3): 1–85. https://doi.org/10.1175/1087-3562(2000)004<0003:PASAOT>2.0.CO;2.

Zhang, Ke, John S. Kimball, Qiaozhen Mu, Lucas A. Jones, Scott J. Goetz, and Steven W. Running. 2009. "Satellite Based Analysis of Northern ET Trends and Associated Changes in the Regional Water Balance from 1983 to 2005." *Journal of Hydrology* 379 (1): 92–110. https://doi.org/10.1016/j.jhydrol.2009.09.047.

Zhao, Maosheng, Steven W. Running, and Ramakrishna R. Nemani. 2006. "Sensitivity of Moderate Resolution Imaging Spectroradiometer (MODIS) Terrestrial Primary Production to the Accuracy of Meteorological Reanalyses." *Journal of Geophysical Research: Biogeosciences* 111 (G1). https://doi.org/10.1029/2004JG000004.